





Evidence for Population-dependent Vertical Motions and the Long-lived Nonsteady Lopsided Milky Way Warp

Xiang Li¹, Hai-Feng Wang^{1,2} , Yang-Ping Luo¹, Martín López-Corredoira^{3,4} , Yuan-Sen Ting^{5,6}, and Žofia Chrobáková⁷

¹Department of Astronomy, China West Normal University, Nanchong 637002, People's Republic of China; hfwang@bao.ac.cn

²CREAF, Centro Ricerche Enrico Fermi, Via Panisperna 89A, I-00184 Roma, Italy

³Instituto de Astrofísica de Canarias, E-38205 La Laguna, Tenerife, Spain

⁴Departamento de Astrofísica, Universidad de La Laguna, E-38206 La Laguna, Tenerife, Spain

⁵Research School of Astronomy & Astrophysics, Australian National University, Cotter Rd., Weston ACT 2611, Australia

⁶School of Computing, Australian National University, Acton ACT 2601, Australia

⁷Faculty of Mathematics, Physics, and Informatics, Comenius University, Mlynská dolina, 842 48 Bratislava, Slovakia

Received 2022 August 19; revised 2022 December 10; accepted 2022 December 12; published 2023 January 27

Abstract

We present a Galactic disk vertical velocity analysis using OB type stars (OB stars), red clump (RC) stars, and main-sequence turnoff (MSTO) stars with different average age populations crossmatched with LAMOST DR5 and Gaia DR3. We show that the vertical velocities of the three populations clearly vary with the Galactocentric distance (R) and the younger stellar population has a stronger increasing trend in general. The bending and breathing modes indicated by the vertical motions are dependent on the populations and vary with spatial locations. These vertical motions may be due to the Galactic warp, or minor mergers, or nonequilibrium of the disk. Assuming the warp is the dominant component, we find that the amplitude of the warp (γ, Z_w) of OB stars (younger population) is larger than that of RC stars (medium population) and the latter is also larger than that for MSTO stars (older population), which is in agreement with other independent analyses of stellar density distribution, and supports that the warp is a long-lived, nonsteady structure and is time evolving. This conclusion is robust whether the line of nodes ϕ_w is fixed or is a free parameter (with ϕ_w being around 3° – $8^\circ.5$ as the best fit). Furthermore, we find that the warp is lopsided with asymmetries along the azimuthal angle (ϕ).

Unified Astronomy Thesaurus concepts: Milky Way disk (1050)

1. Introduction

Disk warp is a common asymmetrical structure found in many disk galaxies (Sánchez-Saavedra et al. 1990; Reshetnikov & Combes 1998; Sánchez-Saavedra et al. 2003). They have different shapes, including the L, S, and U shapes (Kim et al. 2014). Ann & Park (2006) observed in 325 galaxies with 236 (73%) showing warped structures, including 165 S-shaped (51%) and 71-U shaped (22%) structures, which might be caused by different formation mechanisms (Saha & Jog 2006). With the help of near-infrared sky surveys, Gujarro et al. (2010) observed 20 galaxies and found that 13 Galactic disks are warped. As one of the typical disk and spiral galaxies, the Milky Way also has a clearly warped disk, which was first discovered by observations of neutral hydrogen (HI) (Kerr 1957; Westerhout 1957; Bosma 1981; Briggs 1990; Nakanishi & Sofue 2003; Levine et al. 2006b), and was then confirmed by observations of dust (Freudenreich et al. 1994; Marshall et al. 2006), molecular clouds (Grabelsky et al. 1987; Wouterloot et al. 1990; May et al. 1997), and different stellar tracers (Momany et al. 2006; Reylé et al. 2009; Skowron et al. 2019a, 2019b). As can be seen from the view of the edge, the warp bends upward from the Galactic disk plane to the north and downward on the other side (Levine et al. 2006a) and the strength in the north might be greater than that in the south (Skowron et al. 2019a). To date, the origin of the Milky Way warp is still unknown and further studies are needed.

Many mechanisms of the Galactic warp have been proposed in recent years: the inflow of intergalactic matter into the halo (and consequent misalignment of the halo disk that produces the warp through gravitational interaction) (Ostriker & Binney 1989; Quinn & Binney 1992; Jiang & Binney 1999; Bailin & Steinmetz 2003) or directly onto the Galactic disk (López-Corredoira et al. 2002a; Haan & Braun 2014), magnetic fields that exist between galaxies (Battaner & Jiménez-Vicente 1998), interaction between Sagittarius (Bailin 2003) or Magellanic Clouds (Burke 1957; Weinberg & Blitz 2006) with the disk, and the bending instability and self-excited warps or internally driven warps of the Galactic disk (Revaz & Pfenniger 2004; Sellwood & Debattista 2022).

The warp in various Galactic disks might be a long-lived structure as mentioned in Roskar et al. (2010) and Sellwood (2013). López-Corredoira et al. (2014) analyzed the Milky Way warp based on the kinematic model and stellar tracers in the range of 5–16 kpc and suggested that the S-shaped warp is a long-lived structure. However, Poggio et al. (2017) used OB stars to point out that the vertical motions of the Galactic disk cannot be explained by a stable long-lived warp model, and warp may be a transient structure or some phenomena acting on the gaseous component. There is no strict limit on long-lived and short-lived warps. But in this work, we suggest that the long-lived warp is more than a few gigayears old. For instance, a warp that is less than 2 Gyr old can be considered short-lived, whereas a warp that is more than 5 Gyr old can be considered long-lived, and those between 2 and 5 Gyr are of intermediate age.

Using red clump (RC) stars and their ages, Wang et al. (2020b, 2020c) found that warp is a long-lived, nonsteady



Original content from this work may be used under the terms of the [Creative Commons Attribution 4.0 licence](https://creativecommons.org/licenses/by/4.0/). Any further distribution of this work must maintain attribution to the author(s) and the title of the work, journal citation and DOI.

structure, clearly showed that the younger stellar populations are stronger than the older ones. With the high-precision data from Gaia EDR3, Chrobáková et al. (2022) used the star counts and the warp model $z_\omega = [C_\omega R(\text{pc})^{\epsilon_\omega} \sin(\phi - \phi_\omega)]\text{pc}$, where C_ω is the amplitude of the warp and ϕ_ω is the Galactocentric angle defining the warp's line of nodes, to show that supergiants (younger populations) reach a maximum amplitude of $z_\omega = 0.658$ kpc and a minimum amplitude of $z_\omega = -0.717$ kpc at the distance $R = [19.5, 20]$ kpc, while the whole EDR3 population (average old populations) reach a smaller maximum amplitude of $z_\omega = 0.360$ kpc and a minimum of $z_\omega = -0.370$ kpc. These results strongly support the findings of Wang et al. (2020c), that is, the warp is a long-lived, but unstable structure or time evolving.

However, in contrast, Poggio et al. (2018) adopted two stellar tracers with different typical ages (upper main-sequence and giant stars) to reveal that these two populations have similar kinematic characteristics. Similarly, Cheng et al. (2020) explored the relations between stellar velocity and Galactocentric distance, angular momentum, and azimuth, and found that stellar vertical velocity with azimuth and precession are basically similar in different age populations so they found that the warp is from gravitational scenarios. These results are not consistent with the Romero-Gómez et al. (2019) results of warp kinematics using OB stars and RGB stars from Gaia DR2 to show the dependency of Galactic warp on age.

Recently, in order to deepen the understanding of the origin of the warp, Chrobáková & López-Corredoira (2021) further investigated the kinematics of warp based on the same data from Gaia DR2, with the warp model of Chrobáková et al. (2020) to recalculate the warp precession (β). They discovered the value of warp precession of $\beta = 4_{-4}^{+6}$ km s⁻¹ kpc⁻¹, to be compatible with no precession at all. However, before that, Poggio et al. (2020) found a value of warp precession of $\beta = 10.86 \pm 0.03$ (stat.) ± 3.20 (syst.) km s⁻¹ kpc⁻¹ and that the time-varying amplitude model cannot fit the data well. Similarly, Cheng et al. (2020) found a value of warp precession of $\beta = 13.57_{-0.18}^{+0.20}$ km s⁻¹ kpc⁻¹ with data from Gaia DR2 and APOGEE (Majewski et al. 2017). According to Chrobáková & López-Corredoira (2021), the significant detections of precession are due to a wrong assumption of the amplitude of the warp, independent of the stellar populations, which when properly taken into account, removes the necessity of precession.

As is known, warp kinematics and dynamics are mechanisms used to explain the disk oscillations, asymmetries, and Galactoseismology, and as such, the vertical disturbance on the Galactic disk, which could be propagating in the form of bending waves. Based on two simulations in Khachatryan et al. (2022), one with warp caused by gas flowing into the Galactic disk and the other without warp, they found that the simulation with warp can produce a stronger bending wave. A better understanding of warp will promote the understanding of the kinematic structures and gas dynamics of the Galactic disk and Galactoseismology (Wang et al. 2018a, 2018b, 2019, 2020a, 2020b, 2020c; Bland-Hawthorn & Tepper-García 2021; Yu et al. 2021; Wang et al. 2023; Antoja et al. 2022; Yang et al. 2023).

Assuming that the vertical motions could be contributed by warp, modeled as a set of circular rings that are rotated and whose orbit is in a plane with the angle with respect to the Galactic plane, progress has already been made on warp

kinematics in López-Corredoira et al. (2014), Wang et al. (2020b), and Wang et al. (2020c). In this work, different from our previous works, we only chose to use three different stellar populations (OB, RC, and main-sequence turnoff (MSTO) stars) with the distance of LAMOST DR5 (including DR4 MSTO) and Gaia DR3, to explore the warp again mainly from observational points of view in more detail.

This paper is organized as follows. Section 2 describes how we selected the samples and vertical velocity distributions in different stellar populations. Section 3 describes the model and method. We present our results on the time-evolving warp in Section 4, and a discussion is presented in Section 5. Finally, we provide our conclusions in Section 6.

2. Data

In this work, the three different types of stellar tracers (OB, RC, and MSTO stars) adopted are the common stars from the Large Sky Area Multi-Object Fiber Spectroscopic Telescope (LAMOST) Galactic spectroscopic survey (Cui et al. 2012; Deng et al. 2012; Zhao et al. 2012) and the Gaia DR3 astrometric survey. The OB stellar samples can be obtained from Liu et al. 2019. This catalog of 14,344 OB stars has been tested and widely used (Cheng et al. 2019; Wang et al. 2020a; Yu et al. 2021). The distance in this catalog is from Gaia DR3 parallaxes (Gaia Collaboration et al. 2016, 2018). Since we only focus on the range of $R = 8\text{--}14$ kpc, the error in the distance is acceptable. The details of the RC star sample can be found in the work of Ting et al. (2018), which includes a catalog of 175,202 RC stars, with an uncertainty of the distance within 10%. This catalog is also widely used to explore the stellar mass and age (Li et al. 2022). Our MSTO samples and distances are based on the work of Xiang et al. (2017a, 2017b), which includes a catalog of 670,714 MSTO stars, and the error in the distance is estimated to be 10%–30%. The ridge structure has been studied in detail using this sample (Wang et al. 2020a).

Thanks to the latest Gaia DR3, we have obtained more accurate proper motions. The Gaia DR3 catalog (both Gaia EDR3 and the full Gaia DR3) is based on data collected between 2014 July 25 and 2017 May 28 spanning a period of 34 months of data collection. In comparison, Gaia DR2 is based on 22 months of data and Gaia DR1 is based on observations collected in the first 14 months of Gaia's routine operational phase. Gaia DR3 provides us with high-precision position, parallax, and proper motion of 1.5 billion sources with a limiting magnitude of about $G \approx 21$, a bright limit of about $G \approx 3$, and a radial velocity of more than 33 million sources with a limiting magnitude of $G \approx 14$. A full astrometric solution has been performed as a five-parameter solution for 585 million sources and as a six-parameter solution for 882 million sources. The median uncertainties are 0.01–0.02 mas for $G < 15$, 0.05 mas at $G = 17$, 0.4 mas at $G = 20$, and 1.0 mas at $G = 21$ mag. The uncertainty of the proper motion is 0.02–0.03 mas yr⁻¹ for stars with $G < 15$ mag, 0.07 mas yr⁻¹ for stars with $G = 17$ mag, 0.5 mas yr⁻¹ for stars with $G = 20$ mag, and 1.4 mas yr⁻¹ for stars with $G = 21$ mag (Gaia Collaboration et al. 2021, 2022).

Using the following criteria, we obtained the final sample we use in this work:

1. We eliminated the samples without parameters such as distance, radial velocity, and proper motion.

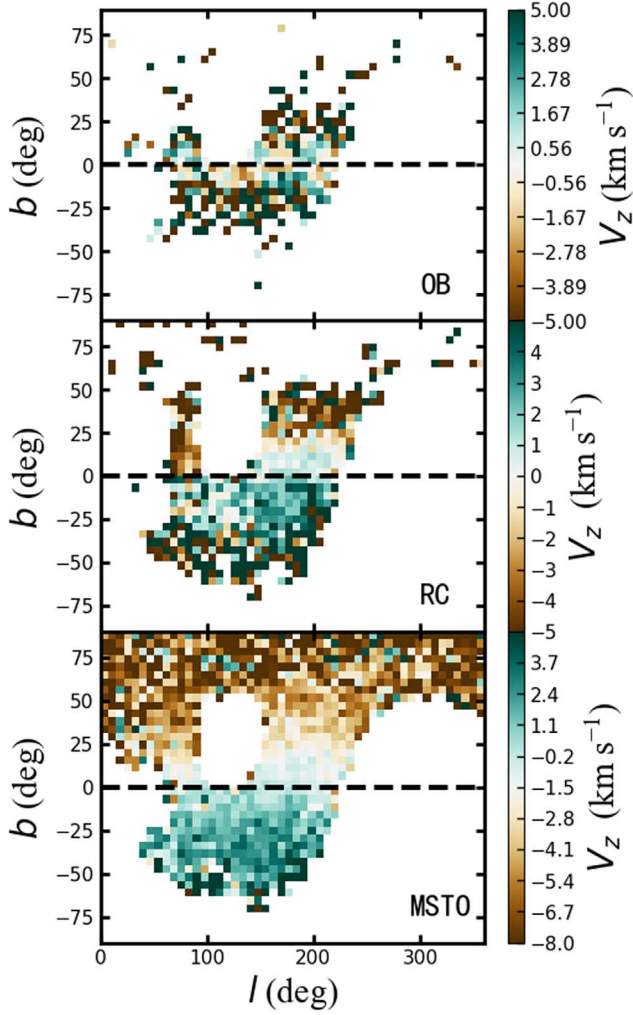


Figure 1. The vertical velocity of different tracers distributed in the celestial coordinates for longitude and latitude. From top to bottom, the panels correspond to the OB, RC, and MSTO samples.

2. We only selected samples in the range of $|Z| < 1$ kpc and $8 \text{ kpc} < R < 14$ kpc.
3. We chose samples with a signal-to-noise ratio greater than 20, and $[\text{Fe}/\text{H}] > -1.3$ dex (for possible halo contamination).
4. The three-dimensional velocity of the samples is in the range of $V_R = [-150, 150] \text{ km s}^{-1}$, $V_\phi = [-50, 350] \text{ km s}^{-1}$, and $V_z = [-150, 150] \text{ km s}^{-1}$.

The three-dimensional velocity we use was obtained by assuming that the location of the Sun is $R_\odot = 8.34$ kpc (Reid et al. 2014) and $Z_\odot = 27$ pc (Chen et al. 2001). We use the Tian et al. (2015) solar motion values of $[U_\odot, V_\odot, W_\odot] = [9.58, 10.52, 7.01] \text{ km s}^{-1}$. The value of the circular speed of the LSR is 238 km s^{-1} (Schonrich 2012). Based on the Cartesian coordinate system, we calculate the 3D velocity, radial distance, vertical height, and azimuth ϕ of the stars using the galpy package (Bovy 2015). Notice that the different solar values and LSR do not change our conclusions. These kinematic parameters are also each described in detail in Wang et al. (2018b), Wang et al. (2019), Wang et al. (2020b), and Wang et al. (2020c).

After applying the above criteria, 529,995 MSTO stars, 85,663 RC stars, and 12,865 OB stars were left and the vertical

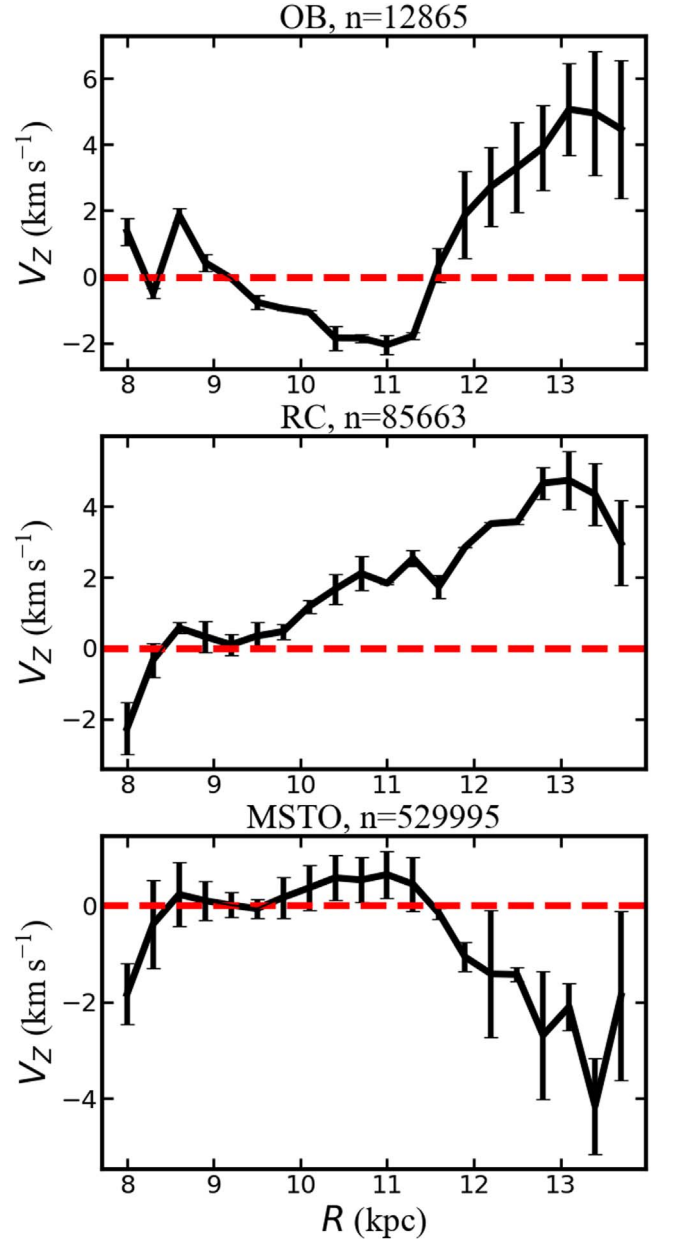


Figure 2. Vertical velocity distributions with radial distance for different stellar populations. The number of samples and population name are labeled at the top of each panel. The horizontal red-dashed line, used to guide the eye, represents the zero velocity value. The three population samples are from the LAMOST survey with different sampling rates and the azimuthal angle of the three populations mainly ranges from -20° to 30° .

velocity distributions in the celestial coordinate system (longitude and latitude) are shown in Figure 1. In this work, we only focus on stars with a Galactocentric distance range of 8–14 kpc and a vertical height of $|Z| < 1$ kpc. In order to clearly present the variation in the vertical velocity (V_z) of different stellar populations with the Galactocentric distance (R), we present the analysis shown in Figure 2 and the stellar population is denoted at the top of each panel. As can be seen from the figure, the vertical velocity of the OB star increases from 2 to 6 km s^{-1} , the vertical velocity of RC stars increases from -2 to 5 km s^{-1} , and the vertical velocity of the MSTO increases from -2 to 2 km s^{-1} and then decreases by 6 km s^{-1} . The distribution of the kinematics of the stellar populations more or less shows the

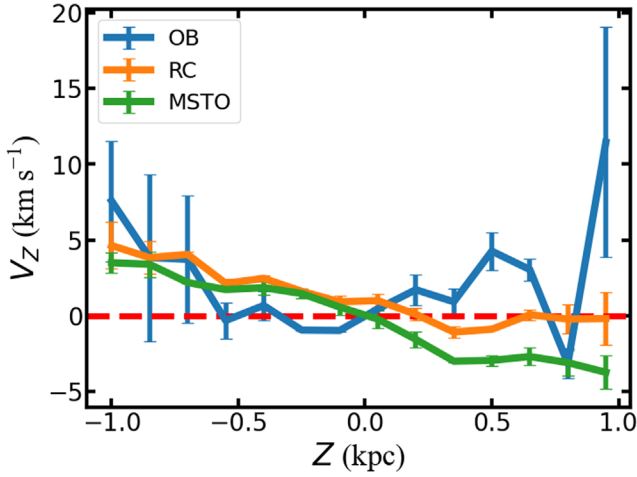


Figure 3. Vertical velocity distributions with vertical height for different stellar populations. Compared to the data shown in Figure 2, the warp signal is not clear at all; however, the vertical asymmetries on the north and south sides are shown here. So the difference in V_Z is not driven by the different distribution in Z .

signal of the warp, and for the overall trend, the younger stellar populations increase faster than the older stellar populations, possibly implying that younger stellar populations have stronger warp features than the older stellar populations. Similarly, vertical velocity distributions with vertical height for different stellar populations are shown in Figure 3. Compared to the illustration shown in Figure 2, the warp signal is not clear but the vertical asymmetries on the north and south sides are shown here.

3. Model

The vertical motions of the (outer) Galactic disk may be related to the warp (Roskar et al. 2010; López-Corredoira et al. 2014; Wang et al. 2018b, 2020b, 2020c; López-Corredoira et al. 2020). As a first approximation, we will assume the observed vertical motions are mainly caused by the warp: a set of circular rings that are rotated, and whose orbit is in a plane with an angle variable with time, $i_w(t)$, with respect to the Galactic plane. See López-Corredoira et al. (2014) for details. We will discuss later whether this approach fits the data or whether other elements (e.g., satellites interactions, and nonequilibrium of the disk) (Wang et al. 2020b; López-Corredoira et al. 2020) are also necessary to explain the vertical velocities. With this assumption, we can explore the evolution of the amplitude (Wang et al. 2020c) and the precession (Cheng et al. 2020; Chrobáková & López-Corredoira 2021) of the warp by vertical velocity, or whether the vertical velocity field will be disturbed (Drimmel et al. 2000). We will also examine the population-dependent bulk motions.

For this work, we use the model designed by Wang et al. (2020c), which is similar to the model (López-Corredoira et al. 2014)

$$V_Z(R > R_\odot) \approx \frac{(R - R_\odot)^\alpha}{R} [\gamma \Omega_{\text{LSR}} \cos(\phi - \phi_w) + \dot{\gamma} R \sin(\phi - \phi_w)], \quad (1)$$

where ϕ_w is the azimuth of the line of nodes (deg), which is the azimuth with the height of the warp equal to zero, γ (kpc^{-1}) is the amplitude of the warp, and $\dot{\gamma}$ ($-\text{d}(\gamma)/\text{d}(\text{age})$, $\text{kpc}^{-1} \text{Gyr}^{-1}$)

describes the evolution of the amplitude of the warp. We also assume a constant rotation speed of $\Omega(R, z) = \Omega_{\text{LSR}} = 238 \text{ km s}^{-1}$ (Schonrich 2012). This may be slightly reduced for high R or high $|z|$ (López-Corredoira et al. 2014), but the order of magnitude does not change, and V_Z is only weakly affected by a change in the rotation speed. α is a power-law constant, and R and ϕ were obtained from observational data points.

First, we assume $\alpha = 1$ (no units) (Reylé et al. 2009), $\phi_w = 5^\circ$ (in the literature, the azimuthal angle has a value between -28° and 18° (López-Corredoira et al. 2002b; Momany et al. 2006; Reylé et al. 2009; Skowron et al. 2019b; Chen et al. 2019)). The results are shown in the next section. Notice that the constant $\alpha = 2$ (kpc^{-1}) has also been tested in our study and the conclusions drawn from the analysis are stable, that is, the amplitude of the sample showed the same decreasing trend as shown in the next section.

In this work, we use a sample with a Galactocentric distance of $R \geq 8 \text{ kpc}$ to obtain the best-fitting results based on a Markov Chain Monte Carlo (MCMC) or EMCEE (Foreman-Mackey et al. 2013) method so we can obtain the likelihood distribution of the vertical velocity profile for the following fitting:

$$\mathcal{L}(V_{\text{obs}}(R_i|Z)|\gamma, \dot{\gamma}, \phi_w) = \prod_i \times \exp \left[-\frac{1}{2} ((V_{\text{obs}}(R_i|Z) - V_{\text{model}}(R_i|Z, \gamma, \dot{\gamma}, \phi_w))^2) \right]. \quad (2)$$

When we obtain the convergent parameters, the MCMC size is $50 \times 3 \times 10,000$, and the step is 50. The values of each parameter (γ , $\dot{\gamma}$, and ϕ_w) based on MCMC fitting will be provided in the next section.

4. Results

4.1. Population-dependent Vertical Bulk Motions

The vertical velocity distributions of three samples in the R – Z plane are shown in Figure 4. It is clear that vertical bulk motions are shown here, but different populations have different patterns. As seen for the distribution of the OB stars, there are *bending modes* with a negative vertical velocity between 10 and 12 kpc, and beyond 12 kpc there is a bending mode with positive velocity, and to our knowledge, this is the first time that this *variable* vertical bulk motion has been found in young populations (left panel). The positive vertical bulk motions or bending modes are shown in the RC star sample (middle panel), and in contrast, for the MSTO population, we could see the positive *breathing mode* between 8 and 9 kpc and positive bending mode between 9 and 12.5 kpc and then the breathing mode between 12.5 and 14 kpc. In general, the bending mode could be described as vertical velocity moving in the same direction and the breathing mode could be described as vertical motions moving in a different direction; more details can be found in Widrow et al. (2014). The bending waves could have been caused by warp with gas infall, as shown in Khachatryan et al. (2022), which is confirmed here by the bending and breathing modes from observations.

So we can claim here that the bending and breathing modes are dependent on the populations and they are evolving with spatial locations. The discovery of the population-dependent vertical motions shown here is vital for a better understanding of the Galactoseismology; however, in this work, we only address the contributions of the warp.

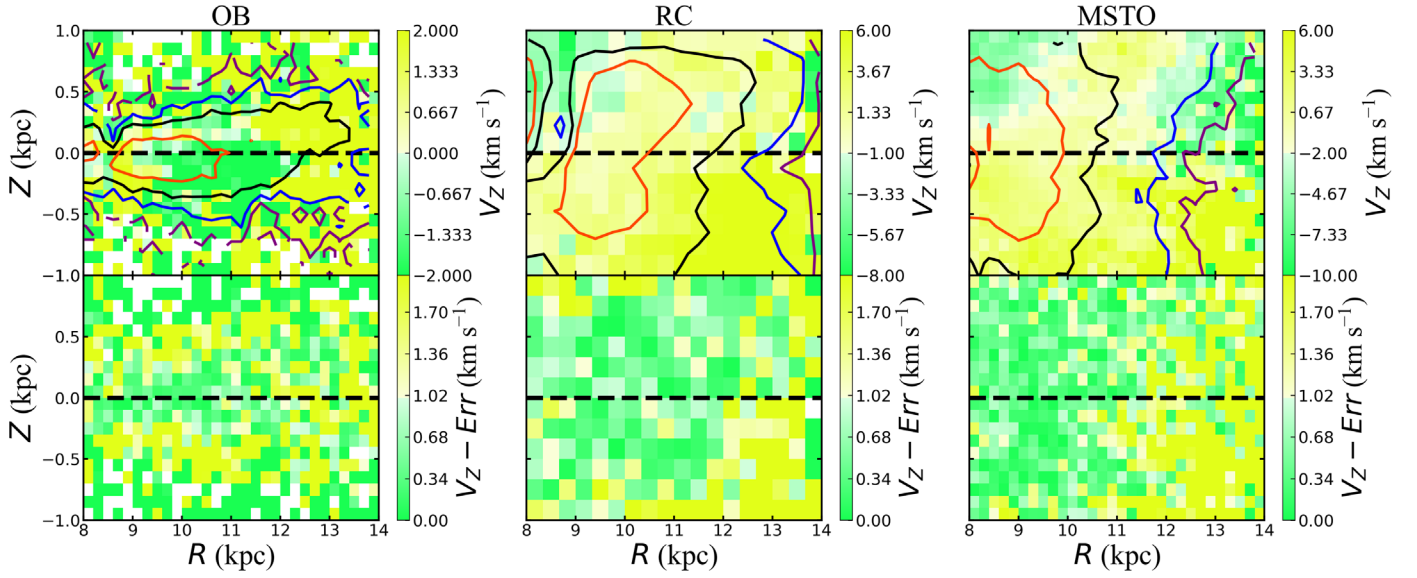


Figure 4. The upper three panels show the vertical velocity distributions of the disk in the R, Z plane, and the bottom three show the errors in the vertical velocity derived by bootstrapping. The OB star is shown in the left panel, the RC star is shown in the middle panels, and the MSTO star is shown in the right panel. The abundant vertical motions or bending and breathing modes are shown here, and the contours for the star counts are superimposed.

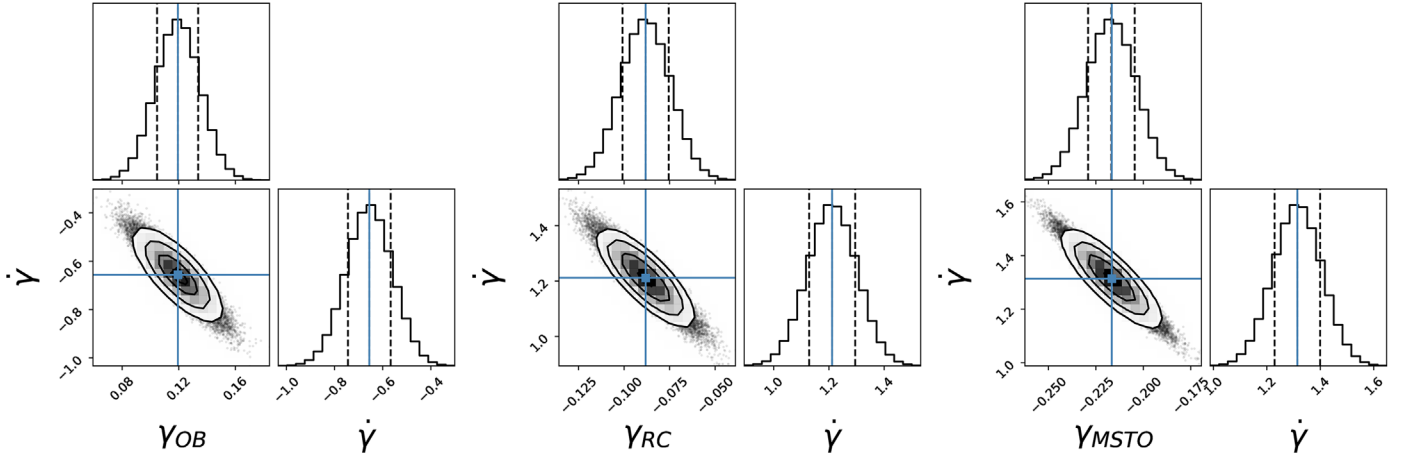


Figure 5. Likelihood distribution of the parameters (γ and $\dot{\gamma}$) drawn from the MCMC simulation for each sample. From left to right, the panels correspond to OB, RC, and MSTO stars. The amplitude of the warp γ of younger populations is larger than that of older populations.

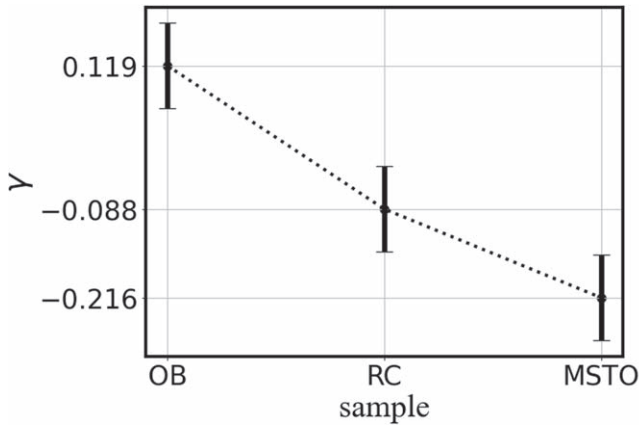


Figure 6. The amplitude of the warp (γ) of different populations obtained by MCMC fitting. The x-axis represents the sample name, and the vertical axis represents the amplitude of the warp. The error bar is derived by bootstrapping and the degeneracies of γ and $\dot{\gamma}$ are shown here. A negative γ for some populations is not expected, implying that the line of nodes should be a free parameter in the fitting process.

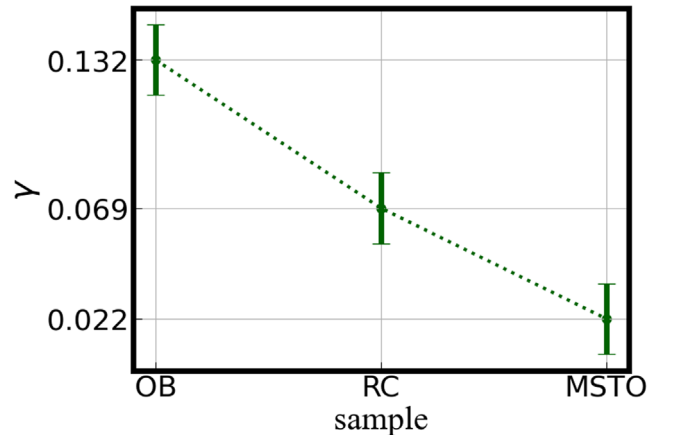


Figure 7. Similar to Figure 6 but with free parameter ϕ_w . The decreasing pattern is similar to that shown in Figure 6.

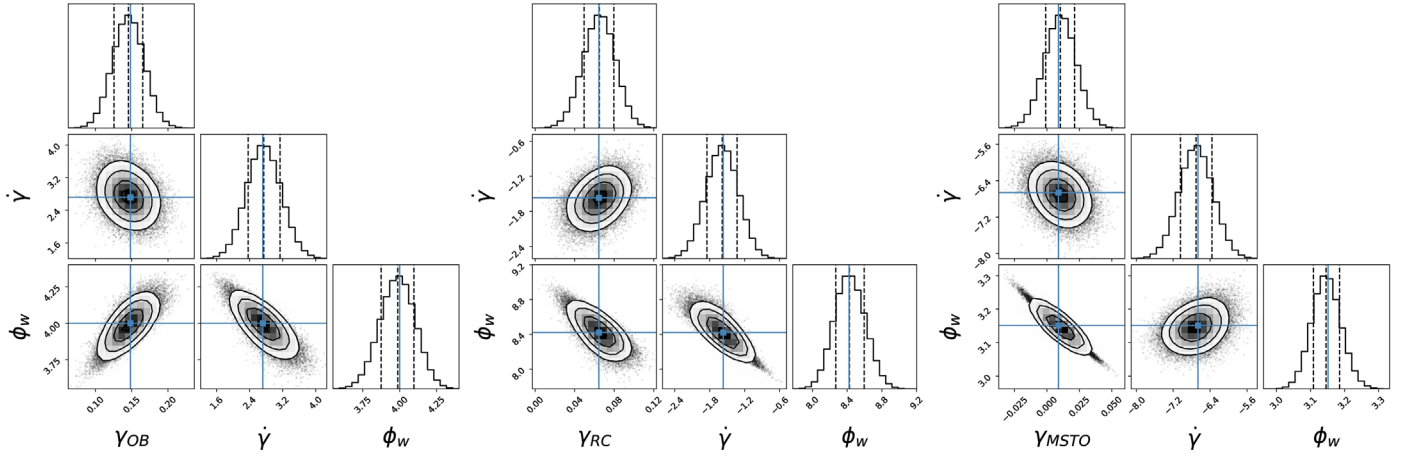


Figure 8. Similar to Figure 5, but ϕ_w is a free parameter, and the likelihood distribution of the parameters (γ , $\dot{\gamma}$, and ϕ_w) is drawn from the MCMC simulation. The amplitude of the warp γ of the younger populations is larger than that of the older populations. Here we can also see that the degeneracy for γ and $\dot{\gamma}$ is broken and different from that shown in Figure 5. Note that $\dot{\gamma}$ is also different in different populations.

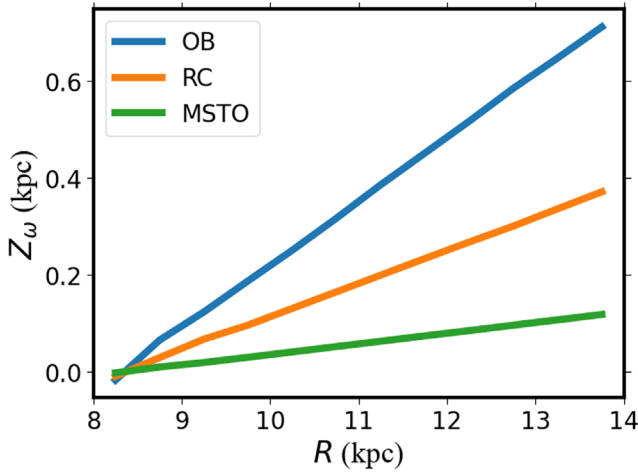


Figure 9. The maximum height caused by the warp is shown here. The x-axis shows the radial distance and the y-axis can be seen as the amplitude of the warp.

4.2. Warp Parameters γ , $\dot{\gamma}$, and ϕ_w

Based on the vertical velocity of the sample we adopted, we conducted the first MCMC fitting under Equation (1) in the model. In this simulation, we assumed $\alpha = 1$ (Reylé et al. 2009) and the azimuth of the line of nodes $\phi_w = 5^\circ$, the fitting result is shown in Figure 5, which has converged quite well. The amplitude of the OB stars is $\gamma_{OB} = 0.119 \text{ kpc}^{-1}$, the amplitude of the RC stars is $\gamma_{RC} = -0.088 \text{ kpc}^{-1}$, and the amplitude of the MSTO stars is $\gamma_{MSTO} = -0.216 \text{ kpc}^{-1}$, which is also shown in Figure 6 with the error derived by bootstrapping. Notice the negative γ shown here implies that a pure sinusoidal warp cannot fit the data perfectly so we need a more robust model in the future; however, we only focus on the relative difference in amplitude, that is, younger populations are stronger than older ones.

Furthermore, negative γ for some populations is not expected when we fix the line of nodes, although we cannot rule out the small possibility that it means that we have detected the opposite warp sign, which is expected in the south. Nevertheless, our analyses may possibly indicate that the line of nodes is different for different populations, and the clear negative degeneracy for γ and $\dot{\gamma}$ will be broken when we set the

line of nodes as a free parameter. Further analysis is shown in Figure 7.

From Figure 6, we can see that the amplitude of the warp (γ) of different stellar populations decreases with the samples with different average ages. Note that, in this work, the typical average age of OB stars is approximately or less than a few hundred megayears (Wang et al. 2020a), that of RC stars is around 3.2 Gyr, and that of MSTO stars is definitely older than that of RC stars with 4.5 Gyr. So the younger stellar population shows a stronger amplitude of warp than the older stellar population here.

At first, we naively assume $\phi_w = 5^\circ$, but know the azimuth of the line of nodes (ϕ_w) obtained by different tracers varies from -28° to 18° (López-Corredoira et al. 2002b; Momany et al. 2006; Reylé et al. 2009; Skowron et al. 2019b; Chen et al. 2019). Therefore, in order to explore whether ϕ_w will affect our conclusions in more detail, we set ϕ_w as a free parameter to fit again.

As shown in Figure 8, we assume $\alpha = 1$ (Reylé et al. 2009) and ϕ_w as a free parameter, and MCMC fitting is carried out again. The values of the amplitudes of the warp are $\gamma_{OB} = 0.132 \text{ kpc}^{-1}$, the amplitude of the RC star is $\gamma_{RC} = 0.069 \text{ kpc}^{-1}$, and the amplitude of the MSTO star is $\gamma_{MSTO} = 0.022 \text{ kpc}^{-1}$, as shown in Figure 7. Similarly, the x-axis represents the sample names and the y-axis represents the amplitude of different stellar populations acquired by model fitting. Obviously, the trend is consistent with that in Figure 6. With the increase in age, the amplitude of the warp decreases, the conclusion of which is also validated by the analysis in Figure 9, which does not the maximum height calculated by Equation (3) in Wang et al. (2020c), but in this work, we adopt $\alpha = 1$ not 2:

$$Z_w(R > R_\odot, \phi = \phi_w + \pi/2) \approx \gamma(R - R_\odot)^\alpha, \quad (3)$$

The height is induced by the warp for different populations and shows that the younger the population is, the stronger the amplitude of the warp is. The values of $\dot{\gamma}$ for the three populations we obtained are not equal to 0, which proves that warp always exists but is not stable. The azimuth of the line of nodes (ϕ_w) of the different stellar populations that we fitted are about 3° – 8° , and the change in ϕ_w is relatively small, which may be caused by the fact that the precession is too small to be detected in all warp models as mentioned in previous works

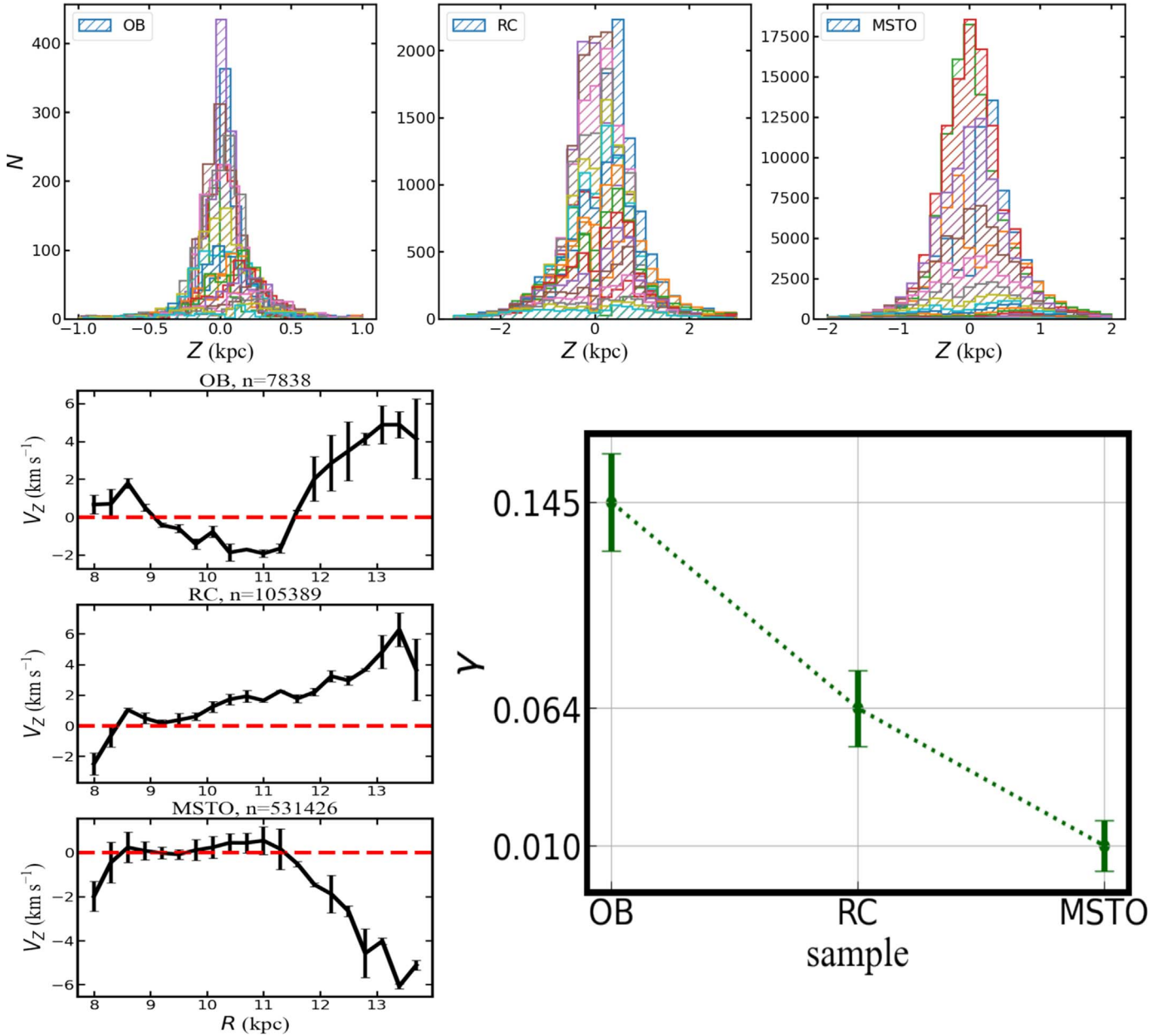


Figure 10. Top left: vertical height distributions for different stellar populations in order to investigate the possible systematics mentioned in Section 4.2. The peak values of the heights are as follows: OB stars $Z_0(R) = [0.0604, 0.0455, -0.022, 0.0170, 0.0133, -0.0055, 0.0052, 0.0074, 0.0159, 0.0181, 0.0255, 0.1117, 0.1442, 0.1642, 0.1837, 0.2156, 0.2186, 0.1426, 0.1523, \text{ and } 0.1120]$; RC stars $Z_0(R) = [0.4525, 0.4973, -0.2908, -0.1939, -0.0483, 0.0528, 0.1054, 0.1158, 0.1429, 0.1522, 0.1939, 0.1690, 0.2185, 0.2182, 0.2642, 0.2507, 0.1642, -0.1402, -0.2015, \text{ and } -0.2118]$; and MSTO stars $Z_0(R) = [0.2709, 0.0714, 0.0072, 0.0356, 0.0437, 0.0491, 0.0553, 0.0725, 0.0979, 0.1783, 0.2589, 0.3433, 0.4197, 0.4944, 0.5243, 0.6012, 0.5973, 0.6271, 0.612, \text{ and } 0.4969]$. Bottom left: vertical velocity distributions with radial distance for different stellar populations, similar to Figure 2. Similar to Figure 7 but we select sample $|Z - Z_0(R)| < 1$ kpc for a test, and as shown, there are no large differences compared to Figure 2. The vertical midplane offsets are not a target of this work.

(López-Corredoira et al. 2002a; Dubinski & Chakrabarty 2009; Jeon et al. 2009). Notice that the line of nodes is expected to be straight within the $R \leq 4.5$ disk scale lengths in some modeling works (Shen & Sellwood 2006; Bland-Hawthorn & Gerhard 2016).

Since the selection is bounded by $|Z| < 1$ kpc, one may wonder if this is introducing a possible systematic bias on the mean V_z . So we select the sample using $|Z - Z_0(R)| < 1$ kpc, for which $Z_0(R)$ is the height of the maximum density at radius R , to test this possibility as shown in Figure 10. The results show that the influence is very minor; see more details in the caption.

4.3. Comparison of the Model and Sample

In order to verify the results obtained by the model fitting, we compare the vertical velocity predicted by the model with the observed data. By using the warp parameters (γ , $\dot{\gamma}$, and ϕ_w) obtained by the model fitting we have the mock data, which can be compared with the observations directly. As shown in Figure 11, the mean vertical velocity distribution is a function of the Galactocentric distance, the blue line represents our model distribution, the yellow line represents the model with $+1\sigma$, the green line represents the model with -1σ , and the black line represents our observational data. The error is

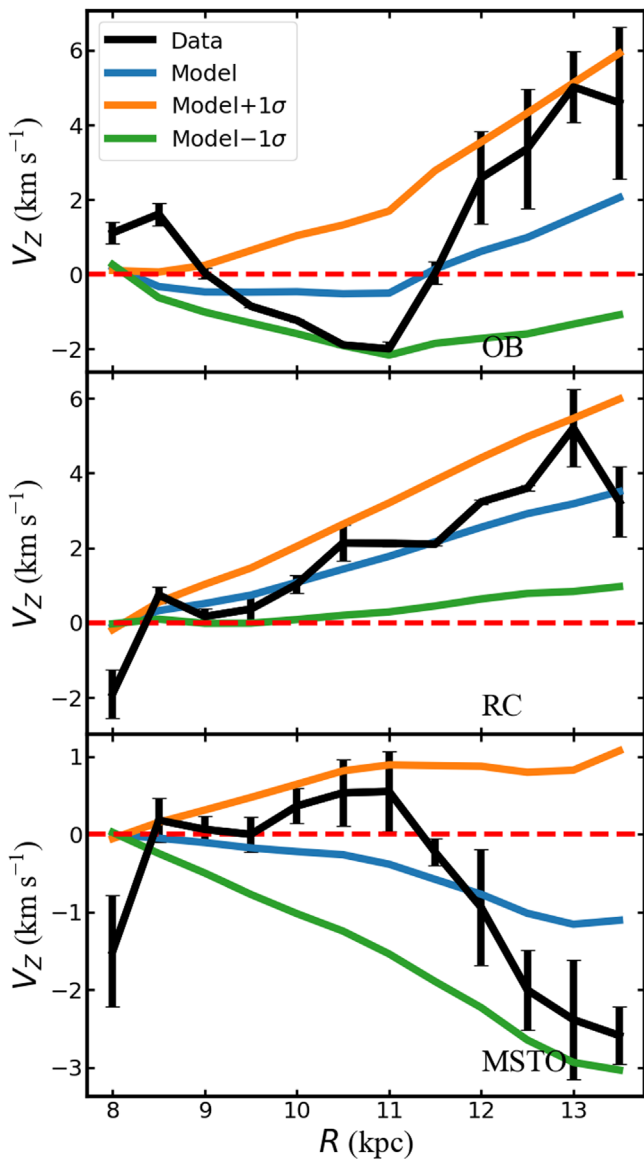


Figure 11. One-dimensional (1D) comparison of the model and data. The blue line represents the model obtained by the MCMC fitting, the orange line represents the model plus 1σ , the green line represents the model minus 1σ , and the black line represents the data distribution. The panels from top to bottom correspond to OB, RC, and MSTO stars, respectively. The error bar is derived by the bootstrapping and the model can be matched well within 1σ .

derived by bootstrapping. From the top to bottom panels, the three samples used in this work are shown, respectively, OB, RC, and MSTO stars.

As can be seen from Figure 11, our model matches well the overall trend of the observed data, at least in the 1σ region. A two-dimensional (2D) comparison of the model and data is shown in Figure 12. The first row denotes the observational vertical velocity distribution on the R and ϕ plane, the second row denotes the observational error derived with bootstrapping, the third row shows the mock data with the model fitting, the fourth row denotes the error in the model, and the fifth row denotes the final error for our model and observations calculated by the model plus the observational error with error propagation. The columns from the left to right correspond to OB, RC, and MSTO stars. Although we can see that there are some differences between the model and the data, due to the

model being a simplified one, and vertical motions might also have been contributed by other mechanisms, the qualitative match is acceptable here.

4.4. Vertical Velocity as Functions of Azimuth

Romero-Gómez et al. (2019) used two different stellar populations from Gaia DR2 (OB stars and red giant branch stars) to find the asymmetry of the mean vertical distance between stars and the Galactic plane, and suggest that the warp is lopsided. Recently, Cheng et al. (2020) combined a Gaia DR2 astrometric solution, StarHorse distance, and stellar abundances from the APOGEE survey to reveal the relations between vertical velocity and azimuth. They found that the vertical velocity increases with the azimuth within 170° and reaches the peak at $\phi \approx 170^\circ$, and then decreases with the azimuth. The increasing and decreasing rates on both sides of the peak are obviously different, which supports the warp being lopsided.

Figure 13 shows the vertical velocity of three stellar populations as functions of azimuth. The top panel shows the distribution of the vertical velocity of all the samples with azimuth. The blue line represents an OB star, the yellow line represents an RC star, and the green line represents an MSTO star, with the error derived by bootstrapping. As can be seen, with the increase in azimuth, the vertical velocity also increases, reaches the peak at $\phi = -10^\circ$ (our definition for the anticenter direction, $\phi = -10^\circ$ is exactly 170°), and then decreases with the increase in azimuth, which is not symmetrical along the peak of the vertical velocity.

In order to further explore this feature of the warp, we divide the three samples into six groups with the distance ($[8-9]$ kpc, $[9-10]$ kpc, $[10-11]$ kpc, $[11-12]$ kpc, $[12-13]$ kpc, and $[13-14]$ kpc). The distributions of the vertical velocity with the azimuth are shown in the bottom three panels of Figure 13, respectively. For the overall trend, we could see that the vertical velocity of the sample increases within $\phi = -10^\circ$, and then, decreases with the increase of azimuth for the MSTO stars, although the pattern is not as clear as in the whole population. The asymmetry around $\phi = -10^\circ$ is not clear for the OB and RC stars but some other asymmetries are detected in different ranges of angles, for example, around $\phi = 10^\circ$, all of which points to some lopsidedness.

In short, based on the evolution of the amplitude and the first derivative of the amplitude, and the vertical velocity patterns along with azimuth. For the assumption that the vertical velocities are produced by the warp, we conclude that this warp is a long-lived, nonsteady, and lopsided structure with an azimuth of the line of nodes of around $3^\circ-8^\circ$, consistent with other works. For the younger stellar populations, it is greater than that of the older stellar populations, which is consistent with the result of Wang et al. (2020c) using RC stars of different ages, which possibly implies that the warp originated from gas infall onto the disk or other hypotheses that suppose that the warp mainly affects the gas, and consequently, younger populations tracing the gas are stronger than older ones.

5. Discussion

The warp contributes vertical nonaxisymmetric velocity patterns and wavelike density in the solar neighborhood and the outer Galactic disk of the Milky Way (Widrow et al. 2012; Carlin et al. 2013; Williams et al. 2013; Xu et al. 2015;

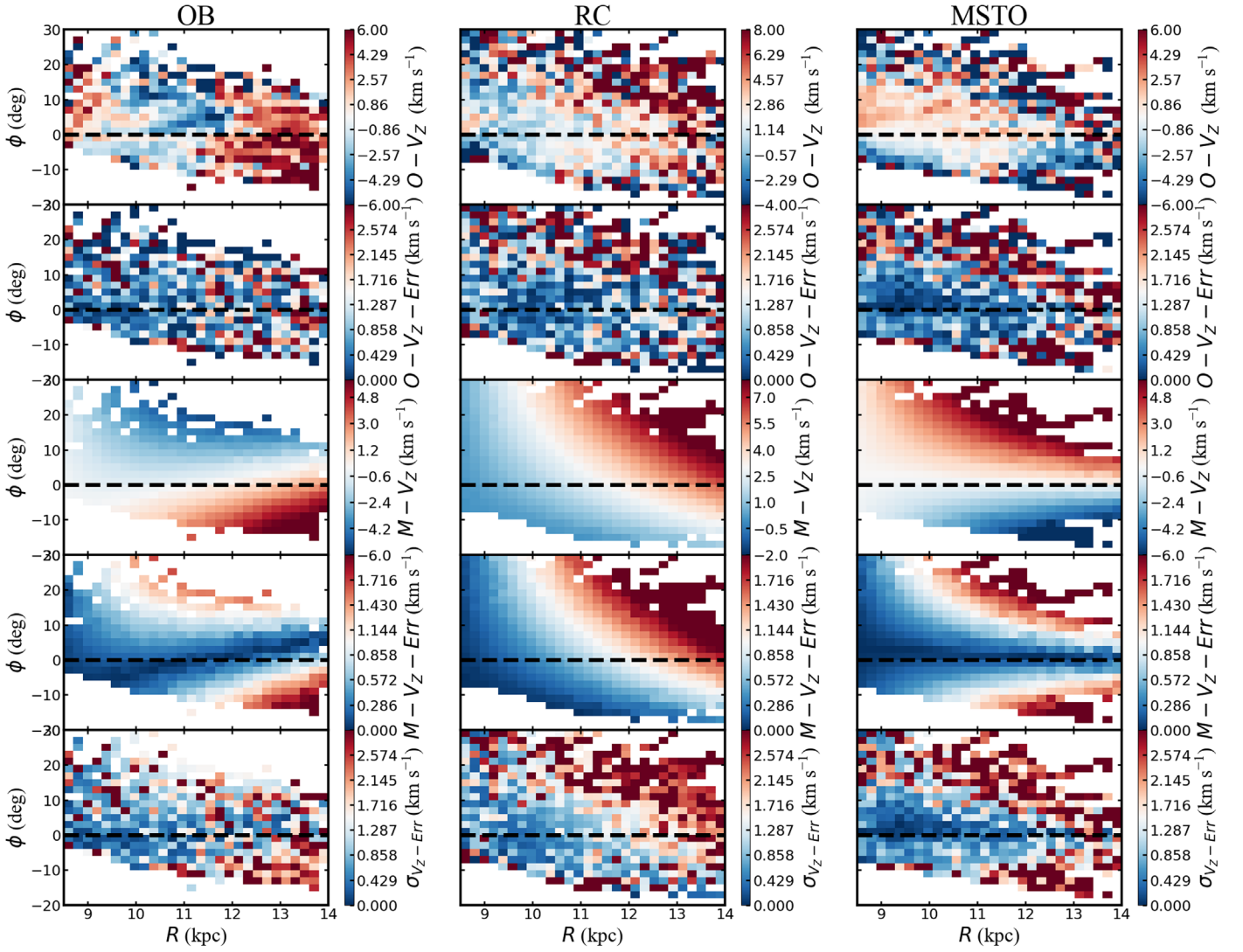


Figure 12. Two-dimensional (2D) comparison of the model and data. (First row) Observational vertical velocity distribution on the R and ϕ plane. (Second row) The observational error using the bootstrap method. (Third row) Mock data with the model fitting. (Fourth row) The distribution of the error in the model. (Fifth row) The final error for our model and the observations are calculated by the model error plus the observational error with error propagation. The columns from the left to right correspond to OB, RC, and MSTO stars. Notice that the quantitative match is not expected and the qualitative comparison is acceptable here.

Pearl et al. 2017; Wang et al. 2018a, 2018b; Carrillo et al. 2018, 2019), but to date, we are still far from ascertaining its exact origin. The Milky Way disk coupling framework for population structure and Galactoseismology was mentioned in Wang et al. (2018b, 2020b). Recently, using N -body simulations with different Sgr masses, Bennett et al. (2022) clearly showed that Sgr is clearly not enough to cause the observed perturbation to the solar neighborhood and multiple mechanisms are needed, which is consistent with our coupling framework.

In recent years, many models, such as the infall of gas, the influence of the intergalactic magnetic field, and the interaction of nearby galaxies, have been proposed as being responsible for the formation of the warp (further details can be found in Section 1). Skowron et al. (2019b) attempted to divide them into two main scenarios: one is the nongravitational mechanisms (the amplitude of the warp is dependent on the stellar age) dominated by, for example, the gas infalling model (friction and collision), the other, for example, are the gravitational mechanisms (the amplitude of the warp is not dependent on the

stellar age) of the influence of satellite galaxies like the Sgr dSph galaxy.

In this work, three kinds of populations from spectroscopic surveys are used to represent different age populations, from younger to older with different average ages. Assuming the vertical velocities produced by the warp, its signal would vary with age as shown in this work: the younger one is stronger and the warp has a clear evolution with age, which strongly supports the warp not being a transient one. In this work, we have conjectured that perhaps both mechanisms contribute to the warp but there are different properties in the different populations and different phase spaces, and this coupling mechanism framework is nontrivial and needs to be further scrutinized in the future. Notice also that to date we are still far from understanding the Sgr dSph galaxy as we are not sure at all about the gas contribution to it and its interaction with the Milky Way (Wang et al. 2022a, 2022b).

Some different observational results were reached by Cheng et al. (2020), who combined Gaia DR2 and StarHorse distance to explore the vertical and radial motion of stars in the Galactic

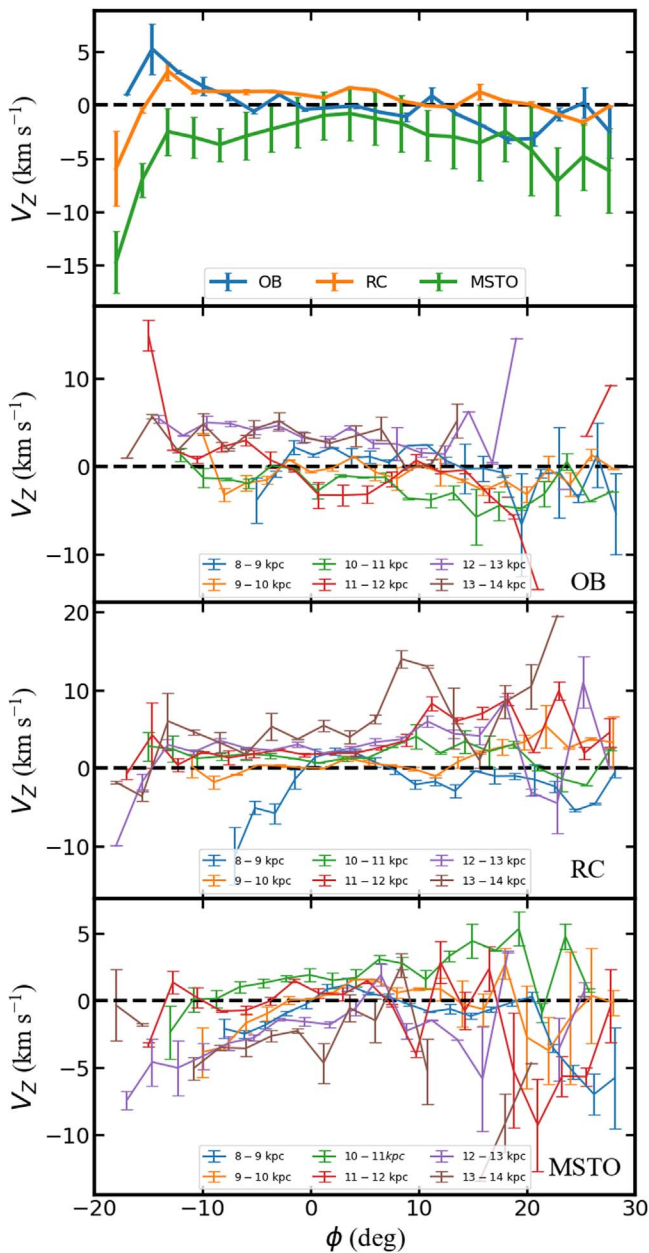


Figure 13. The vertical velocity distribution along with the azimuth. The first panel shows the distributions of all of the samples. The bottom three panels show the different distributions of the samples at different radial distances, and the top to bottom panels show those of the OB, RC, and MSTO stars. The increase is within -10° and the peak is at $\phi \approx -10^\circ$, and then decreases with the azimuth as shown in the top panel, implying that the warp is lopsided.

disk, and in the meantime, they established a warp model to support that warp is caused by the action of external gravity due to that there is no evolution of the precession rate. However, Chen et al. (2019) used 1339 classical Cepheids to explore the Galactic disk and found that the young stellar populations showed a stronger warp feature, which was also found by Chrobáková et al. (2020) with the help of Gaia DR2. More importantly, when we look carefully at the pattern of vertical velocity versus ϕ azimuth, we find that our decreasing trend is weaker than that in Cheng et al. (2020), which will be confirmed by our new Gaia DR3 results, implying that the lopsidedness might be not so strong as found in Cheng et al. (2020).

Nonetheless, vertical velocities alone cannot be used to derive the properties of the warp because there are other possible dynamical causes for non-null vertical velocities (López-Corrodoira et al. 2020). They might be generated by external perturbations or mergers, or by the fact the Galactic disk is a nonequilibrium system. The disk may not have reached equilibrium since its creation or because external forces, such as the Sgr dwarf galaxy, might perturb it, etc. We have found that a pure warp model with variable amplitude of time and the epoch of formation of the stellar population fits reasonably well with the observed features (see Figure 11), which may indicate that the warp has an important average contribution to the vertical kinematics component. Moreover, details such as the exact dependence on the stellar population or the lopsidedness could be due to secondary factors such as mergers, nonequilibrium, or others. And one needs analyses different from the kinematics, mainly stellar density distribution (e.g., Chrobáková et al. 2022) to corroborate that the warp is really dependent on the age.

6. Conclusions

In short, our analysis of the warp has some similar results or implications (time-evolving warp for amplitude) to other previous works (Liu et al. 2017; Chen et al. 2019; Romero-Gómez et al. 2019; Wang et al. 2020b, 2020c; Chrobáková et al. 2020), but there are also differences from some others (Poggio et al. 2018; Cheng et al. 2020; Poggio et al. 2020), which may be attributed to the different samples and models adopted in different works. Moreover, the warp is lopsided, which has been mentioned in many works (Amôres et al. 2017; Poggio et al. 2018; Romero-Gómez et al. 2019; Cheng et al. 2020) and is also confirmed here, but due to the range of the azimuth of our sample being smaller than 50° , we cannot clearly show this feature as we do for others. Furthermore, the asymmetry of the warp in the northern and southern disk is also an interesting point of view, which has been presented in many works (Momany et al. 2006; Reylé et al. 2009; Amôres et al. 2017; Chrobáková et al. 2022). We plan to continue to explore all of these in future works using more samples and other warp models.

Based on the three different kinds of stellar populations (OB \approx a few to a few hundred megayears, RC stars \approx 3 Gyr, MSTO stars \approx 4 Gyr) from the common stars of LAMOST DR5 and Gaia DR3, we investigate the evolution of warp amplitude, the azimuth of the line of nodes, and the changes in vertical velocity with the azimuth angles. We clearly find the amplitude of the warp, obtained from the kinematic model, of the younger stellar populations, is larger than that of the older stellar populations with temporal evolution. Moreover, the azimuth of the line of nodes is about 3° – 8° and the vertical velocity is a function of azimuth, which supports that the warp is lopsided but perhaps not as strong as the results of recent APOGEE work. Nonetheless, these conclusions are conditioned on a predominance of the warp in the vertical velocities, and that the effect of minor merger or nonequilibrium is much smaller.

Furthermore, we first discovered that the vertical bulk motions are different in different populations, and the bending and breathing modes are population dependent, which provide more constraints on the theoretical models, and we invite the theorist community to further investigate the disk bending and breathing, and the relations to warp, mergers, or nonequilibrium scenarios.

This analysis of vertical velocities in terms of a warp, together with other independent analyses with different methods and data, favors a scenario in which the warp is a long-lived nonstationary lopsided structure. As prospects, in future work, we will make full use of different kinds of stellar samples with better sampling and sky coverage and different models to unveil more of the mysteries of the S-shape Milky Way warp (e.g., torque and precession), as more Gaia DR3 works will be finished in the future.

We would like to thank the anonymous referee and Francesco Sylos Labini for the very helpful and insightful comments. We acknowledge the National Key R&D Program of China (Nos. 2021YFA1600401 and 2021YFA1600400). H.F.W. acknowledges the support from the project Complexity in self-gravitating systems of the Enrico Fermi Research Center (Rome, Italy) and science research grants from the China Manned Space Project with Nos. CMS-CSST-2021-B03 and CMS-CSST-2021-A08. L.Y.P. is supported by the National Natural Science Foundation of China (NSFC) under grant No. 12173028, the Chinese Space Station Telescope project: CMS-CSST-2021-A10, the Sichuan Science and Technology Program (grant No. 2020YFSY0034), the Sichuan Youth Science and Technology Innovation Research Team (grant No. 21CXTD0038), the Major Science and Technology Project of the Qinghai Province (grant No. 2019-ZJ-A10), and the Innovation Team Funds of China West Normal University (grant No. KCXTD2022-6). Y.S.T. acknowledges financial support from the Australian Research Council through DECRA Fellowship DE220101520. H.F.W. looks forward to the plan “Mapping the Milky Way (Disk) Population Structures and Galactoseismology (MWDPSG) with large sky surveys” in order to establish a theoretical framework in the future to unify/partly unify the global picture of the disk structures and origins with a possible comprehensive distribution function. The Guo Shou Jing Telescope (the Large Sky Area Multi-Object Fiber Spectroscopic Telescope, LAMOST) is a National Major Scientific Project built by the Chinese Academy of Sciences. Funding for the project has been provided by the National Development and Reform Commission. LAMOST is operated and managed by the National Astronomical Observatories, Chinese Academy of Sciences. This work has also made use of data from the European Space Agency (ESA) mission Gaia (<https://www.cosmos.esa.int/gaia>), processed by the Gaia Data Processing and Analysis Consortium (DPAC; <https://www.cosmos.esa.int/web/gaia/dpac/consortium>). Funding for the DPAC has been provided by national institutions, in particular, the institutions participating in the Gaia Multilateral Agreement.

ORCID iDs

Hai-Feng Wang  <https://orcid.org/0000-0001-8459-1036>
 Martín López-Corredoira  <https://orcid.org/0000-0001-6128-6274>

References

- Amôres, E. B., Robin, A. C., & Reylé, C. 2017, *A&A*, 602, A67
 Ann, H. B., & Park, J.-C. 2006, *NewA*, 11, 293
 Antoja, T., Ramos, P., López-Guitart, F., et al. 2022, *A&A*, 668, A61
 Bailin, J. 2003, *ApJL*, 583, L79
 Bailin, J., & Steinmetz, M. 2003, *Ap&SS*, 284, 701
 Battaner, E., & Jiménez-Vicente, J. 1998, *A&A*, 332, 809
 Bennett, M., Bovy, J., & Hunt, J. A. S. 2022, *ApJ*, 927, 131
 Bosma, A. 1981, *AJ*, 86, 1825
 Bovy, J. 2015, *ApJS*, 216, 29
 Briggs, F. H. 1990, *ApJ*, 352, 15
 Bland-Hawthorn, J., & Gerhard, O. 2016, *ARA&A*, 54, 529
 Bland-Hawthorn, J., & Tepper-García, T. 2021, *MNRAS*, 504, 3168
 Burke, B. F. 1957, *AJ*, 62, 90
 Carlin, J. L., DeLaunay, J., Newberg, H. J., et al. 2013, *ApJL*, 777, L5
 Carrillo, I., Minchev, I., Kordopatis, G., et al. 2018, *MNRAS*, 475, 2679
 Carrillo, I., Minchev, I., Steinmetz, M., et al. 2019, *MNRAS*, 490, 797
 Chen, B., Stoughton, C., Smith, J. A., et al. 2001, *ApJ*, 553, 184
 Chen, X., Wang, S., Deng, L., et al. 2019, *NatAs*, 3, 320
 Cheng, X., Anguiano, B., Majewski, S. R., et al. 2020, *ApJ*, 905, 49
 Cheng, X., Liu, C., Mao, S., & Cui, W. 2019, *ApJL*, 872, L1
 Chrobáková, Ž., & López-Corredoira, M. 2021, *ApJ*, 912, 130
 Chrobáková, Ž., Nagy, R., & López-Corredoira, M. 2020, *A&A*, 637, A96
 Chrobáková, Ž., Nagy, R., & López-Corredoira, M. 2022, *A&A*, 664, A58
 Cui, X.-Q., Zhao, Y.-H., Chu, Y.-Q., et al. 2012, *RAA*, 12, 1197
 Deng, L.-C., Newberg, H. J., Liu, C., et al. 2012, *RAA*, 12, 735
 Drimmel, R., Smart, R. L., & Lattanzi, M. G. 2000, *A&A*, 354, 67
 Dubinski, J., & Chakrabarty, D. 2009, *ApJ*, 703, 2068
 Foreman-Mackey, D., Hogg, D. W., Lang, D., & Goodman, J. 2013, *PASP*, 125, 306
 Freudenreich, H. T., Berriman, G. B., Dwek, E., et al. 1994, *ApJL*, 429, L69
 Gaia Collaboration, Brown, A. G. A., Vallenari, A., et al. 2018, *A&A*, 616, A1
 Gaia Collaboration, Brown, A. G. A., Vallenari, A., et al. 2021, *A&A*, 649, A1
 Gaia Collaboration, Prusti, T., de Bruijne, J., et al. 2016, *A&A*, 595, A1
 Gaia Collaboration, Vallenari, A., Brown, A. G. A., et al. 2022, arXiv:2208.00211
 Grabelsky, D. A., Cohen, R. S., Bronfman, L., Thaddeus, P., & May, J. 1987, *ApJ*, 315, 122
 Gujarro, A., Peletier, R. F., Battaner, E., et al. 2010, *A&A*, 519, A53
 Haan, S., & Braun, R. 2014, *MNRAS*, 440, L21
 Jeon, M., Kim, S. S., & Ann, H. B. 2009, *ApJ*, 696, 1899
 Jiang, I.-G., & Binney, J. 1999, *MNRAS*, 303, L7
 Kerr, F. J. 1957, *AJ*, 62, 93
 Khachatryan, T., Beraldo e Silva, T., Debattista, V. P., & Daniel, K. J. 2022, *MNRAS*, 512, 3500
 Kim, J. H., Peirani, S., Kim, S., et al. 2014, *ApJ*, 789, 90
 Levine, E. S., Blitz, L., & Heiles, C. 2006a, *ApJ*, 643, 881
 Levine, E. S., Blitz, L., & Heiles, C. 2006b, *Sci*, 312, 1773
 Li, Q.-D., Wang, H.-F., Luo, Y.-P., et al. 2022, *ApJS*, 262, 20
 Liu, Z., Cui, W., Liu, C., et al. 2019, *ApJS*, 241, 32
 Liu, C., Tian, H.-J., & Wan, J.-C. 2017, in IAU Symp. 321, Formation and Evolution of Galaxy Outskirts (Cambridge: Cambridge Univ. Press), 6
 López-Corredoira, M., Abedi, H., Garzón, F., & Figueras, F. 2014, *A&A*, 572, A101
 López-Corredoira, M., Betancort-Rijo, J., & Beckman, J. E. 2002a, *A&A*, 386, 169
 López-Corredoira, M., Cabrera-Lavers, A., Garzón, F., & Hammersley, P. L. 2002b, *A&A*, 394, 883
 López-Corredoira, M., Garzón, F., Wang, H.-F., et al. 2020, *A&A*, 634, A66
 Majewski, S. R., Schiavon, R. P., Frinchaboy, P. M., et al. 2017, *AJ*, 154, 94
 May, J., Alvarez, H., & Bronfman, L. 1997, *A&A*, 327, 325
 Marshall, D. J., Robin, A. C., Reylé, C., Schultheis, M., & Picaud, S. 2006, *A&A*, 453, 635
 Momany, Y., Zaggia, S., Gilmore, G., et al. 2006, *A&A*, 451, 515
 Nakanishi, H., & Sofue, Y. 2003, *PASJ*, 55, 191
 Ostriker, E. C., & Binney, J. J. 1989, *MNRAS*, 237, 785
 Pearl, A. N., Newberg, H. J., Carlin, J. L., & Smith, R. F. 2017, *ApJ*, 847, 123
 Poggio, E., Drimmel, R., Andrae, R., et al. 2020, *NatAs*, 4, 590
 Poggio, E., Drimmel, R., Lattanzi, M. G., et al. 2018, *MNRAS*, 481, L21
 Poggio, E., Drimmel, R., Smart, R. L., Spagna, A., & Lattanzi, M. G. 2017, *A&A*, 601, A115
 Quinn, T., & Binney, J. 1992, *MNRAS*, 255, 729
 Reid, M. J., Menten, K. M., Brunthaler, A., et al. 2014, *ApJ*, 783, 130
 Reshetnikov, V., & Combes, F. 1998, *A&A*, 337, 9
 Revaz, Y., & Pfenniger, D. 2004, *A&A*, 425, 67
 Reylé, C., Marshall, D. J., Robin, A. C., & Schultheis, M. 2009, *A&A*, 495, 819
 Romero-Gómez, M., Mateu, C., Aguilar, L., Figueras, F., & Castro-Ginard, A. 2019, *A&A*, 627, A150
 Roskar, R., Debattista, V. P., Brooks, A. M., et al. 2010, *MNRAS*, 408, 783
 Saha, K., & Jog, C. J. 2006, *A&A*, 446, 897
 Sánchez-Saavedra, M. L., Battaner, E., & Florido, E. 1990, *MNRAS*, 246, 458

- Sánchez-Saavedra, M. L., Battaner, E., Guijarro, A., López-Corredoira, M., & Castro-Rodríguez, N. 2003, *A&A*, **399**, 457
- Schonrich, R. 2012, *MNRAS*, **427**, 274
- Sellwood, J. A. 2013, in *Planets, Stars and Stellar Systems*, ed. T. D. Oswalt & G. Gilmore, Vol. 5, 923
- Sellwood, J. A., & Debattista, V. P. 2022, *MNRAS*, **510**, 1375
- Skowron, D. M., Skowron, J., Mróz, P., et al. 2019a, *AcA*, **69**, 305
- Skowron, D. M., Skowron, J., Mróz, P., et al. 2019b, *Sci*, **365**, 478
- Shen, J., & Sellwood, J. A. 2006, *MNRAS*, **370**, 2
- Tian, H.-J., Liu, C., Carlin, J. L., et al. 2015, *ApJ*, **809**, 145
- Ting, Y.-S., Hawkins, K., & Rix, H.-W. 2018, *ApJL*, **858**, L7
- Wang, H.-F., Liu, C., Xu, Y., et al. 2018a, *MNRAS*, **478**, 3367
- Wang, H.-F., López-Corredoira, M., Carlin, J. L., et al. 2018b, *MNRAS*, **477**, 2858
- Wang, H.-F., Carlin, J. L., Huang, Y., et al. 2019, *ApJ*, **884**, 135
- Wang, H.-F., Huang, Y., Zhang, H.-W., et al. 2020a, *ApJ*, **902**, 70
- Wang, H.-F., López-Corredoira, M., Huang, Y., et al. 2020b, *MNRAS*, **491**, 2104
- Wang, H.-F., López-Corredoira, M., Huang, Y., et al. 2020c, *ApJ*, **897**, 119
- Wang, H.-F., Chrobáková, Ž., López-Corredoira, M., & Sylos Labini, F. 2023, *ApJ*, **942**, 12
- Wang, H.-F., Hammer, F., Yang, Y.-B., & Wang, J.-L. 2022a, *ApJL*, **940**, L3
- Wang, H.-F., Yang, Y.-B., Hammer, F., & Wang, J.-L. 2022b, arXiv:2204.08542
- Weinberg, M. D., & Blitz, L. 2006, *ApJL*, **641**, L33
- Westerhout, G. 1957, *BAN*, **13**, 201
- Widrow, L. M., Barber, J., Chequers, M. H., & Cheng, E. 2014, *MNRAS*, **440**, 1971
- Widrow, L. M., Gardner, S., Yanny, B., Dodelson, S., & Chen, H.-Y. 2012, *ApJL*, **750**, L41
- Williams, M. E. K., Steinmetz, M., Binney, J., et al. 2013, *MNRAS*, **436**, 101
- Wouterloot, J. G. A., Brand, J., Burton, W. B., et al. 1990, *A&A*, **230**, 21
- Xiang, M., Liu, X., Shi, J., et al. 2017a, *ApJS*, **232**, 2
- Xiang, M.-S., Liu, X.-W., Yuan, H.-B., et al. 2017b, *MNRAS*, **467**, 1890
- Xu, Y., Newberg, H. J., Carlin, J. L., et al. 2015, *ApJ*, **801**, 105
- Yu, Y., Wang, H.-F., Cui, W.-Y., et al. 2021, *ApJ*, **922**, 80
- Yang, P., Wang, H.-F., Luo, Z.-Q., Tepper-García, T., & Luo, Y.-P. 2023, *AJ*, *in press*, arXiv:2205.09227
- Zhao, G., Zhao, Y.-H., Chu, Y.-Q., Jing, Y.-P., & Deng, L.-C. 2012, *RAA*, **12**, 723